

# Calculation of the Equilibrium Evolution of the ZaP Flow Z-Pinch Using a Four-Chord Interferometer

Sean D. Knecht, *Member, IEEE*, Raymond P. Golingo, Brian A. Nelson, and Uri Shumlak, *Member, IEEE*

**Abstract**—A four-chord interferometer and measurements from an array of surface-mounted magnetic probes were used in conjunction with equations of radial heat conduction and radial force balance to calculate the equilibrium evolution of a pinch plasma in the ZaP flow Z-pinch. A multiple shooting method was used to solve the nonlinear coupled differential equation system, with ohmic heating and bremsstrahlung radiation as sources and sinks, respectively. Data from a single ZaP pulse are reported including profiles of magnetic field and temperature and their evolution. Profiles are dominated by high thermal conductivity near the axis which quickly decreases with radius. This is due to the plasma being weakly magnetized near the axis which increases thermal conductivity and flattens the temperature profile, but strongly magnetized near the characteristic radius, significantly reducing thermal conductivity and resulting in a large temperature gradient. The equilibrium evolution indicates that plasmas in ZaP heat and compress with increasing current as a result of magnetic compression during the quiescent period.

**Index Terms**—Equilibrium evolution, interferometry, pinch oscillation, plasma heating, Z-pinch.

## I. INTRODUCTION

MEASURING the evolution of the electron density in a plasma experiment is critical to understanding the behavior of the plasma, including equilibrium properties and associated fluctuations. A common method of measuring the electron density as a function of time is interferometry. Interferometry is a widely used diagnostic technique on many different plasma experiments including field-reversed configurations (FRCs) [1], spheromaks [2], tokamaks [3], [4], stellarators [5], capillary discharges [6], and plasmoids from coaxial plasma accelerators [7].

These systems often consist of multiple chords which measure chord-integrated electron density. The chord-integrated measurements must be inverted to determine electron density profiles,  $n_e(r)$  [8], [9]. The electron density profile evolution from interferometry can be used in concert

with other diagnostics to reconstruct other equilibrium properties of the plasma [10].

This paper describes a method in which two of the temporally evolving equilibrium properties of the ZaP flow Z-pinch [11]–[14], magnetic field and temperature, are calculated using electron density measurements from a four-chord interferometry system to completely describe the Z-pinch MHD equilibrium. Interferometry and magnetic probe measurements are coupled with the equations of radial force balance and radial heat conduction. The effects of ohmic heating and bremsstrahlung radiation are taken into account. Density profile measurements at a single temporal point in the ZaP flow Z-pinch have been previously reported using holographic interferometry [9] and spectroscopy [15]. In addition to offering spatially resolved measurements, four-chord interferometry provides temporally resolved density profiles during a single pulse, which allows a more detailed study of the evolution of the plasma.

## II. ZaP FLOW Z-PINCH EXPERIMENTAL CONFIGURATION

The Z-pinch is a simple magnetic confinement configuration, consisting of a column of plasma between two conductors. The plasma is in equilibrium when radial force balance is satisfied, i.e., when the pressure gradient is balanced by magnetic force and magnetic tension as described by

$$\mathbf{j} \times \mathbf{B} = \nabla p \quad (1)$$

where  $\mathbf{j}$  is the current density,  $\mathbf{B}$  is the magnetic field,  $p = k_B(n_e T_e + n_i T_i)$ ,  $k_B$  is Boltzmann's constant,  $n_e$  and  $n_i$  are the electron and ion densities, and  $T_e$  and  $T_i$  are the electron and ion temperatures, respectively.

The ZaP flow Z-pinch experiment is shown in Fig. 1 and consists of coaxial conductors with no externally generated magnetic fields, similar to a Marshall gun design [16]. The outer conductor extends beyond the end of the inner conductor and constitutes the pinch assembly region. During a pulse, neutral gas is injected radially from the inner and outer conductors midway down the inner conductor, and capacitor banks are discharged across the inner conductor and the outer conducting wall, ionizing the gas; typical gases are hydrogen, helium, and methane. The Lorentz force accelerates the plasma axially until it reaches the end of the inner conductor, where the pinch assembles along the machine axis. The current sheet continues moving down the outer conductor until it reaches the end wall where the assembly is completed resulting in

Manuscript received August 22, 2014; revised November 21, 2014; accepted May 7, 2015. Date of publication May 25, 2015; date of current version August 7, 2015. This work was supported in part by the National Nuclear Security Administration under Grant DE-NA0001860 and in part by the U.S. Department of Energy under Grant DE-FG02-04ER54756. (*Corresponding author: Sean D. Knecht.*)

S. D. Knecht is with the Applied Research Laboratory, Pennsylvania State University, State College, PA 16801 USA (e-mail: sdk149@psu.edu).

R. P. Golingo, B. A. Nelson, and U. Shumlak are with the Aerospace and Energetics Research Program, University of Washington, Seattle, WA 98195 USA (e-mail: golingo@aa.washington.edu; nelson@ee.washington.edu; shumlak@uw.edu).

Color versions of one or more of the figures in this paper are available online at <http://ieeexplore.ieee.org>.

Digital Object Identifier 10.1109/TPS.2015.2431973

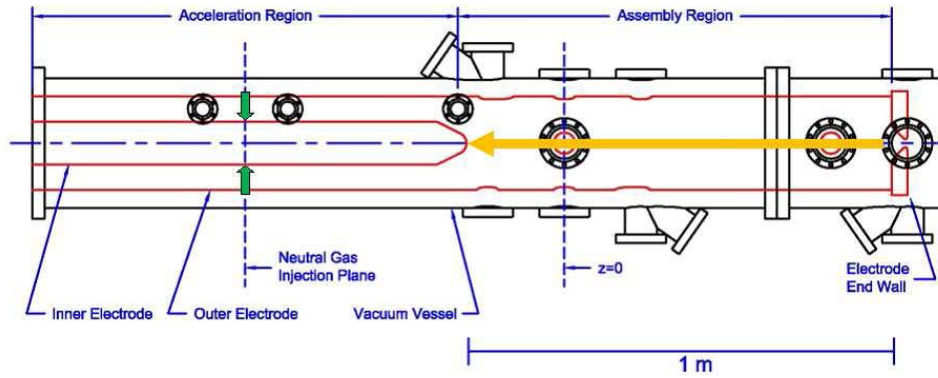


Fig. 1. ZaP flow Z-pinch geometry. ZaP consists of a 1-m coaxial gun with no externally generated magnetic fields, coupled to a 1-m pinch assembly region. Gas is injected radially midway down the inner conductor from both the inner and outer conductor prior to capacitor bank discharge. The arrows indicate the position of the current sheet and the direction of current flow immediately after ionization (green) and after pinch formation (yellow). The measurements described in this paper are made at the  $z = 0$ -m plane. A 1-m scale is included for reference.

TABLE I  
ZaP OPERATING PARAMETERS

Parameter	Value
Accelerator Length (m)	1
Outer Conductor Radius (m)	0.10
Inner Conductor Radius (m)	0.08
Pinch Radius, $a$ (m)	0.01
Pinch Length (m)	1
Peak Current (kA)	300–400
Electron Density ( $\text{m}^{-3}$ )	$10^{22}$ – $10^{23}$
Temperature, $T_e, T_i$ (eV)	50–125
Magnetic Field (T)	0.5–2
Quiescent Period ( $\mu\text{s}$ )	30–70

a pinch with a long axial extent ( $\approx 1$  m) and an embedded axial flow. The arrows in Fig. 1 indicate the positions of the current sheet and the direction of current flow immediately after ionization (green) and after pinch formation (yellow). The location  $z = 0$  m is the primary diagnostic location in this paper.

Measurements and analysis have indicated that ZaP flow Z-pinch plasmas remain stable as a result of sheared axial flows that are generated during the pinch formation process [11], [12], [17], [18]. Instability growth times for static plasmas with similar plasma and magnetic field parameters are on the order of 10 ns. ZaP plasmas are observed to be stable for thousands of times longer than the instability growth times [13], [14]. It is hypothesized that the heating of the Z-pinch plasma is a result of adiabatic compression [19] during the pinch formation process. ZaP operational parameters are shown in Table I. Methane ( $\text{CH}_4$ ) was used for the pulse described here. Methane is used on ZaP to introduce an artificial carbon impurity to facilitate spectroscopic measurements. It has been observed experimentally that pinches produced using hydrogen and methane are dynamically indistinguishable in ZaP.

#### A. ZaP Diagnostics

ZaP utilizes a number of diagnostics to measure plasma equilibrium and stability. For this paper, the two primary systems of interest are a magnetic probe array and the four-chord interferometer. Surface-mounted magnetic probes are located

in the outer conductor and measure the change in azimuthal magnetic field as a function of time,  $dB_\theta/dt$ . Analog integration of this signal provides the magnetic field evolution,  $B_\theta$ . Four azimuthal arrays of surface-mounted magnetic probes are located at  $z = -0.25$  m,  $z = 0$  m,  $z = 0.35$  m, and  $z = 0.70$  m. The array at  $z = -0.25$  m has six probes and the other arrays have eight probes uniformly spaced at  $45^\circ$  increments. The azimuthal arrays are used to determine the stability characteristics of the pinch at those locations. Fourier decomposition of the data yields the amplitudes of the azimuthal magnetic field,  $B_m$ . The  $m = 0$  mode is the average magnetic field measured by the probes,  $m = 1$  indicates the radial offset of the current centroid from the axis of the machine,  $m = 2$  is a measure of the ellipticity of the current distribution, and  $m = 3$  is the triangularity of the current distribution. The  $m = 1$  mode is the fastest growing and highest amplitude of the asymmetric modes, identifies the current centroid location, and defines the ZaP stability criterion. When the normalized  $m = 1$  mode,  $(B_1/B_0)$ , is less than 0.2, the radial displacement of the current centroid from the machine axis is less than 0.01 m [20]. ZaP pulses exhibit a period of time during which the normalized value drops below 0.2 and the frequency of magnetic fluctuations decreases. This is called the stable, or quiescent, period.

ZaP utilizes a four-chord helium–neon (He–Ne) Mach-Zehnder heterodyne, quadrature interferometer for chord-integrated electron density measurements. The He–Ne laser beam ( $6328 \text{ \AA}$ ) enters an acousto-optic modulator (Bragg cell) and two exiting beams are utilized; one at the original laser frequency (zeroth order) and one with a 40 MHz offset (first order). For each of the four chords, a scene beam passes through the  $z = 0$  m port of the experiment. Upon exiting the experiment through a port diametrically opposite, the scene beam is recombined with a reference beam and a quadrature detector measures the optical phase difference. A schematic of a single chord in ZaP is shown in Fig. 2. The measured phase difference is directly proportional to the chord-integrated electron density, as expressed by

$$\phi = \frac{\omega}{2cn_c} \int n_e dl \quad (2)$$

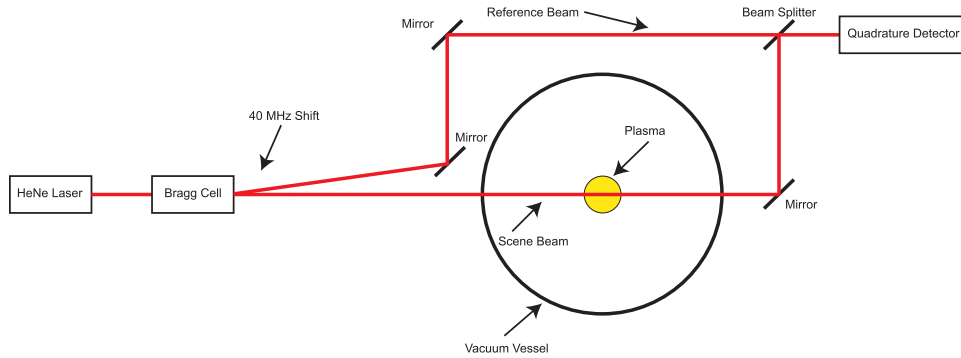


Fig. 2. Schematic of the axial view of a single chord of the ZaP He-Ne interferometry system. A He-Ne laser beam (6328 Å) enters an acousto-optic modulator (Bragg cell) and two exiting beams are utilized: one at the original frequency and a second beam with a 40 MHz offset. One beam passes through the experiment and the plasma (scene beam) and the other bypasses the plasma (reference beam). The beams are combined and sent to a quadrature detector which measures the phase difference between the beams, which is directly proportional to the chord-integrated electron density.

where  $c$  is the speed of light,  $\omega$  is the frequency of the laser light,  $n_e$  is the electron number density,  $n_c = (\omega^2 m_e \epsilon_0 / e^2)$  is the cutoff plasma density of the laser,  $\epsilon_0$  is the permittivity of free space,  $e$  is the elementary electron charge, and  $m_e$  is the rest mass of an electron.

Additional chords for the interferometer are produced by passing the beams through beam splitters. The diagnostic has four chords that can be placed at various locations on the experiment. The configuration used in this paper utilizes four chords at different impact parameters for measuring the density profile at a single  $z$ -location,  $z = 0$  m.

The measured chord-integrated density as a function of time often exhibits high-frequency oscillations that are a combination of signal noise and density fluctuations about the equilibrium density profile. These oscillations are not relevant to determining the equilibrium density profile of the pinch, which evolves on a slower time scale. The chord-integrated densities as a function of time are filtered using a process called empirical mode decomposition (EMD) [21] (see the Appendix for more information). Interferometry data are decomposed as lower frequency mean behavior with high-frequency oscillations superimposed. Data that follow show chord-integrated densities with the high-frequency oscillations filtered out.

### III. INTERFEROMETRY ANALYSIS

The four interferometry chords were placed at  $z = 0$  m at different impact parameters. Fig. 3 shows a schematic example of the four-chord interferometry setup. The yellow circle is an axial view of the Z-pinch plasma column. The black dot indicates the location of the current centroid determined from the azimuthal magnetic probe array. The four colored horizontal lines indicate the locations of the four interferometry chords. The locations remain constant relative to the machine axis at  $y = 0.1$  cm (blue),  $y = -0.6$  cm (green),  $y = -1.3$  cm (red), and  $y = -2.0$  cm (black). Fig. 4 shows the magnetic data at  $z = 0$  m for a representative pulse. The resulting chord-integrated density data as a function of time and the  $y$ -location of the current centroid for this pulse, determined from the azimuthal magnetic probe array, are shown in Fig. 5. The colors in Fig. 5 correspond to the colors

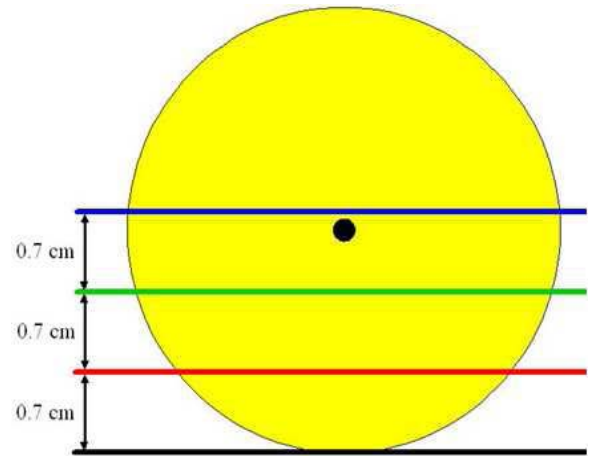


Fig. 3. Schematic of the four-chord interferometer setup. The yellow circle signifies an axial view of the pinch with the four interferometer scene beams passing through at impact parameters that are spaced 7 mm apart. The locations remain constant relative to the machine axis at  $y = 0.1$  cm (blue),  $y = -0.6$  cm (green),  $y = -1.3$  cm (red), and  $y = -2.0$  cm (black). The colors of the scene beams are consistent with the colors of the data traces in Fig. 5. The black dot indicates the location of the current centroid, which is determined from the azimuthal magnetic probe array data.

in Fig. 3. The data indicate a well-defined pinch with an observable density gradient during the quiescent period, which is represented by the red vertical lines from 32 to 55  $\mu$ s. The interferometry chord closest to the current centroid (blue) has the highest chord-integrated density. Chords further from the current centroid show decreasing chord-integrated densities. Error bars are on the order of  $10^{-3}$  T for the magnetic field data and  $10^{19}$   $m^{-2}$  for the density data [13].

The chord-integrated data and the location of the current centroid are analyzed to determine the radial density profile evolution throughout the plasma pulse. The plasma density is assumed to be azimuthally symmetric about the current centroid. The analysis requires the chord-integrated density to monotonically decrease with distance from the current centroid. Fig. 6 shows an example of the chord-integrated density as a function of impact parameter relative to the machine axis with the four points indicating magnitudes of

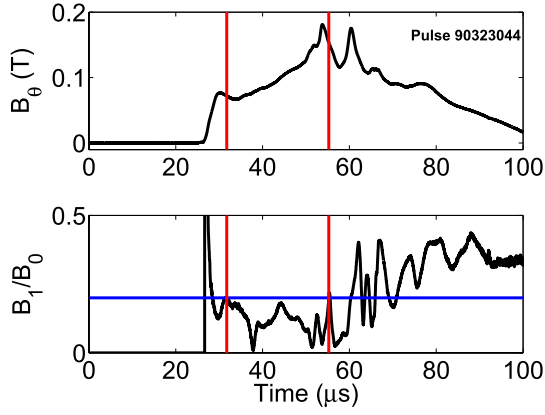


Fig. 4. Magnetic field data for representative operating conditions, showing the average azimuthal magnetic field (top plot) and the normalized  $m = 1$  mode (bottom plot). Pulses are characterized by a smoothly rising magnetic field during the quiescent period. The beginning and end of the quiescent period, defined by a sustained period with  $B_1/B_0 \leq 0.2$  (blue line), are indicated by the red vertical lines. The peak of the magnetic field typically precedes the end of the quiescent period.

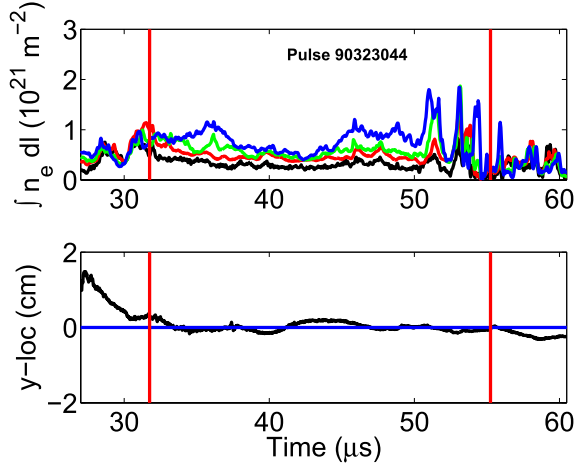


Fig. 5. Interferometry data for representative operating conditions (top plot) and calculated  $y$ -location of the current centroid (bottom plot). During the quiescent period, the data show a well-defined pinch with an observable density gradient, which is indicated by the chord located closest to the machine axis having the highest magnitude (blue) and chords further from the machine axis having monotonically decreasing values. The location of the plasma density peak agrees with the  $y$ -location of the current centroid determined from the azimuthal magnetic probe array data which indicates a current centroid located within a few millimeters of the machine axis throughout the quiescent period.

the chord-integrated data and the vertical line indicating the location of the current centroid. The horizontal blue lines indicate the estimated measurement uncertainty of the chord locations, which is  $\pm 1$  mm. The beams are approximately 3–4 mm in diameter and the location of the beam midpoints can be visually resolved to approximately  $\pm 1$  mm. The vertical error bars are smaller than the symbol size. The mirror point is the reflection of the datum measured on the right side of the axis, which results from the assumption of azimuthal symmetry about the current centroid.

As a starting point for the analysis, a pressure profile is guessed to fit a Bennett equilibrium pressure profile [22],

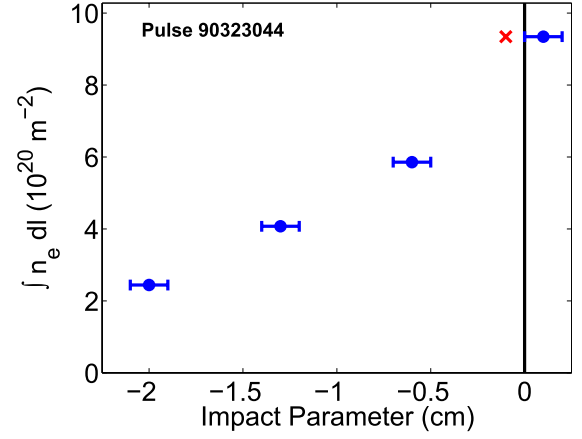


Fig. 6. Example chord-integrated density data at time,  $t = 49.8 \mu\text{s}$ . The analysis requires chord-integrated density to decrease monotonically with distance from the current centroid. Impact parameter is with respect to the machine axis. The indicated mirror point (x) is the reflection of the datum to the right of the axis.

which has a well-studied analytic solution [23]

$$p = \frac{\mu_0 I_{\text{pinch}}^2}{8\pi^2} \frac{a^2}{(r^2 + a^2)^2} \quad (3)$$

where  $\mu_0$  is the permeability of free space,  $I_{\text{pinch}}$  is the total pinch current, and  $a$  is the characteristic radius of the pinch.

The density and temperature profiles are initially guessed to have the same radial dependence. This produces a Lorentzian density profile

$$n_e(r) = \frac{n_0 a^2}{r^2 + a^2} \quad (4)$$

where  $n_0$  is the density at  $r = 0$  m. The assumed profile extends to the outer conductor wall,  $r_w$ .

Integrating this equation along the path length of an interferometry chord from the wall of the outer conductor yields an expression for the chord-integrated density profile

$$\int n_e|_{y_i} dl = \frac{2n_0 a^2}{\sqrt{y_i^2 + a^2}} \tan^{-1} \left( \frac{l}{\sqrt{y_i^2 + a^2}} \right) \quad (5)$$

where  $y_i$  is the impact parameter relative to the current centroid and  $l = (r_w^2 - y_i^2)^{1/2}$  is the chord length. The four chord-integrated points fitted to this chord-integrated profile using a nonlinear least-squares fit method using  $a$  and  $n_0$  as fit parameters.

Fig. 7 shows the chord-integrated data points and the chord-integrated fit at a single time for the given pulse,  $t = 49.8 \mu\text{s}$ . Fig. 7 also shows the resulting electron density profile for three times during the pulse: during the first expansion,  $t = 37.5 \mu\text{s}$ ; near the time of largest pinch radius,  $t = 42.7 \mu\text{s}$ ; and near the time of greatest compression,  $t = 49.8 \mu\text{s}$ . The chord-integrated data indicate that the Lorentzian density profile is a reasonable fit. The blue points are the experimentally measured chord-integrated values as a function of impact parameter relative to the current centroid. The shaded areas are the range of values after displacing the measured location of the current centroid between  $\pm 1$  mm

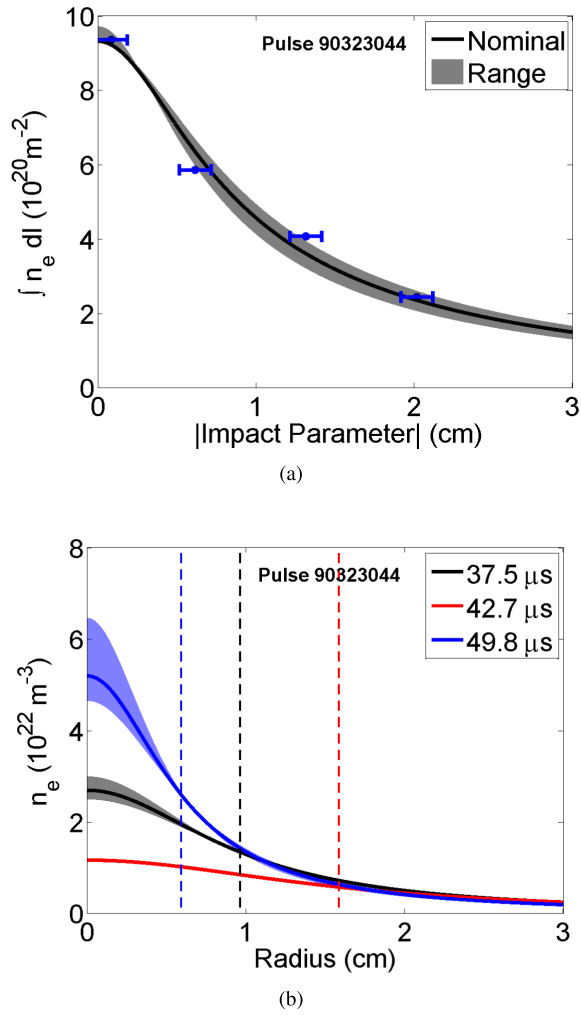


Fig. 7. Chord-integrated fit at  $t = 49.8 \mu\text{s}$  and electron density profiles at three different times. (a) Chord-integrated data points fitted with a nonlinear least-squares method. Impact parameter is with respect to the current centroid. Blue points are experimentally measured; blue horizontal lines are the estimated measurement uncertainty of chord locations ( $\pm 1$  mm). (b) Lorentzian electron density profile calculated from the values of  $a$  and  $n_0$  fit to the chord-integrated data for three times during the pulse. Shaded areas in both plots indicate the fits resulting from displacing the measured location of the current centroid between  $\pm 1$  mm. Vertical dashed lines indicate the characteristic radius.

to account for uncertainties in the chord locations and the assumption of coincidence between the current centroid location and the pinch axis. This is done by producing chord-integrated fits for a range of shifted centroid values  $[-1, 1]$  mm. The values that produce the highest and lowest magnitudes of linear density,  $N = \int n_e dA$ , where  $A$  is the cross-sectional area of the pinch, are used to calculate this uncertainty range.

Fig. 8 shows the evolution of the values of the characteristic radius and the on-axis density as a function of time during the quiescent period. The gaps in the data are due to failure to meet the condition of monotonically decreasing values of chord-integrated density with distance from the current centroid or failure to converge for the numerical method described in Section IV. The red lines are regression fits of the data to a first-order function in time. The shaded black areas are

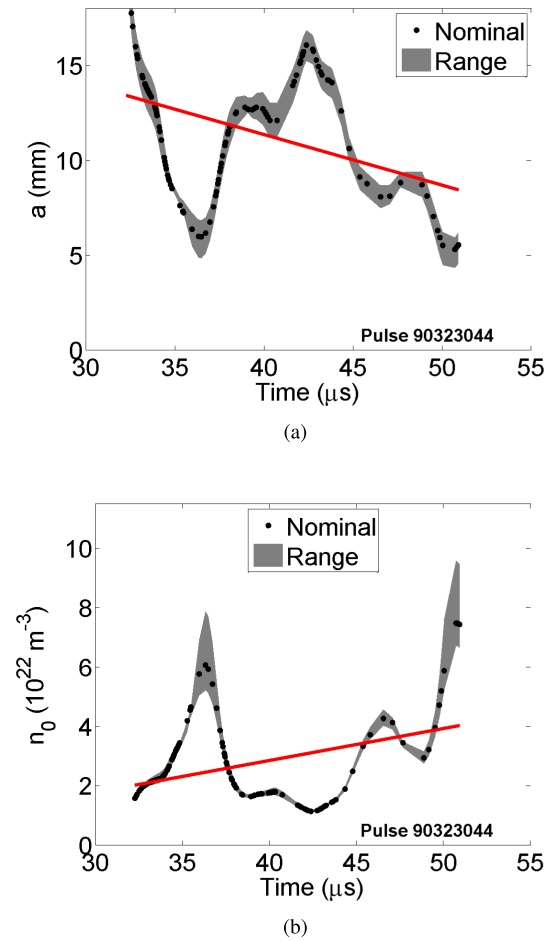


Fig. 8. Characteristic pinch radius and peak density as a function of time. (a) Overall trend is a decrease in the size of the pinch with increasing time. (b) On-axis density is anticorrelated with the pinch size, as expected. The pinch is compressing as a function of time. The red lines are regression fits of the data to a first-order function in time. Shaded black areas are with the current centroid displaced between  $\pm 1$  mm. Uncertainty is larger at approximately 36 and 50  $\mu\text{s}$  due to the smaller characteristic radius which is approaching the size of the uncertainty levels.

the data with the current centroid shifted between  $\pm 1$  mm. Uncertainty is largest at approximately 36 and 50  $\mu\text{s}$  due to the smaller characteristic radius which is approaching the size of the uncertainty levels. The overall behavior of this pulse suggests that the pinch was being compressed as a function of time with the characteristic radius of the pinch decreasing by up to a factor of three, from 15 to 5 mm, and the resulting peak electron density increasing to a peak of  $7.5 \times 10^{22} \text{ m}^{-3}$ . Large magnitude oscillations are observed in the characteristic radius of the pinch with primary minima occurring at 36 and 51  $\mu\text{s}$  and a maximum at  $t \approx 43 \mu\text{s}$ . This behavior can be interpreted as one cycle of a periodic expansion and contraction of the pinch with a 15- $\mu\text{s}$  period. Further cycles cannot be observed in the presented pulse due to the quiescent period ending soon after 51  $\mu\text{s}$ , as indicated in Fig. 5, but the decreasing radius starting at 33  $\mu\text{s}$  and the short period of increasing radius after 51  $\mu\text{s}$  suggest that other expansion/contraction cycles are possible. Section V discusses how the Z-pinch formation process can result in periodic contraction and expansion of

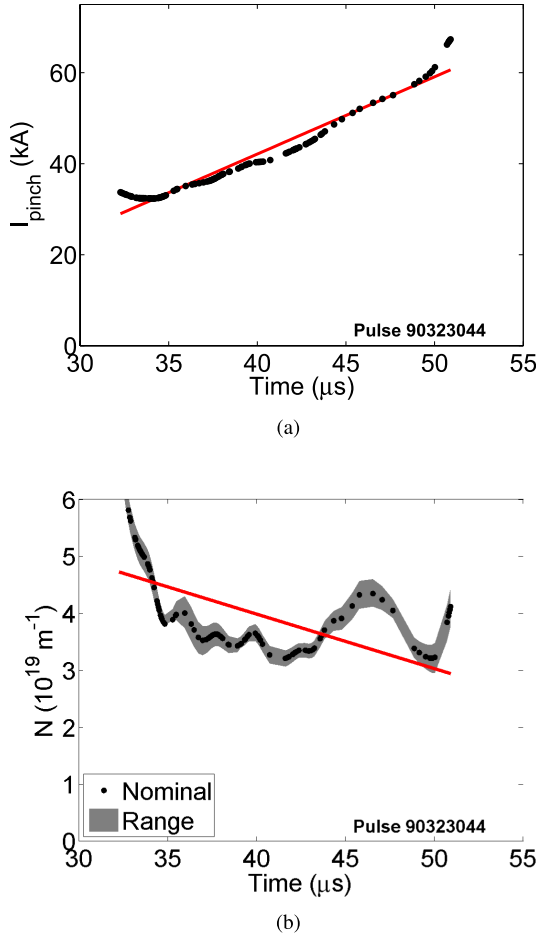


Fig. 9. Pinch current and linear density as a function of time. (a) Pinch current is increasing as a function of time, consistent with the compression of the pinch. (b) Linear density is approximately constant as a function of time, resulting in an increase in peak electron density due to compression of the pinch. Shaded black areas in (b) are with the current centroid displaced between  $\pm 1$  mm.

the pinch. The second observed minimum is smaller than the first indicating that in addition to the periodic behavior of the pinch size, an overall compressional effect is observed.

This compression is expected from Fig. 9, which shows the total pinch current at  $z = 0$  m increasing, from 30 to 70 kA, and the linear density remaining relatively constant as a function of time, at approximately  $4 \times 10^{19} \text{ m}^{-1}$ . Shifting of the measured current centroid location has little effect on the calculated linear density. A total mass of the pinch can be calculated from this linear density, assuming that the dominant carbon impurity is doubly ionized CIII, the length of the pinch is  $L = 1$  m, and that the pinch is axially uniform as  $m_{\text{pinch}} = (N_C m_C + N_H m_p)L = 2.67 N L m_p = 1.8 \times 10^{-7} \text{ kg}$ , where  $m_p = 1.67 \times 10^{-27} \text{ kg}$  is the mass of a proton,  $m_C = 12 m_p$  is the mass of a carbon atom,  $N_H$  is the linear density of hydrogen ions, and  $N_C$  is the linear density of carbon ions. The total pinch current is calculated using Ampere's law with the measured magnetic field at  $z = 0$  m.

The overall evolution of the density profile is more readily evident using a contour plot of electron density as a function of radius and time as shown in Fig. 10. The contours shown

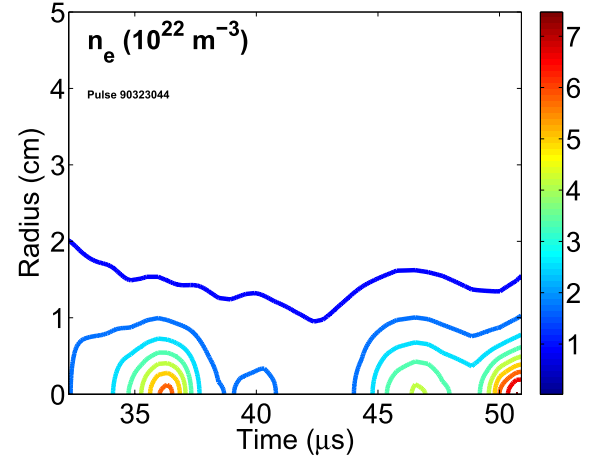


Fig. 10. Contour plot of electron density for representative operating conditions. Electron density contours as a function of radius and time indicate the overall compression of the pinch. Contours shown are for the measured location of the current centroid only and do not take the location uncertainty into account.

are for the measured location of the current centroid only and do not take the location uncertainty into account.

#### IV. CALCULATIONS OF MAGNETIC FIELD AND TEMPERATURE PROFILES

The equations of conservation of energy and radial force balance can be used to calculate profiles for the magnetic field and temperature of the pinch, using the calculated density profiles at a given temporal point. According to the MHD model, the conservation of energy equation is

$$\frac{3}{2} \frac{\partial p}{\partial t} + \frac{3}{2} \nabla \cdot p \mathbf{v} + p \nabla \cdot \mathbf{v} + \nabla \cdot \mathbf{q} = S \quad (6)$$

where  $p$  is the plasma pressure,  $\mathbf{v}$  is the plasma velocity,  $\mathbf{q}$  is the heat flux, and  $S$  are sources and sinks in the system. The first term of (6) represents the time rate of change of the internal energy density, the second term represents the convection losses, the third term is energy loss due to fluid expansion, and the fourth term is loss due to thermal conduction [24].

A steady-state equilibrium is considered, such that the first term in (6) vanishes, assuming that the equilibration time which is the Alfvén time,  $\tau_A = a/V_A$ , is faster than the characteristic time of radial motion,  $a/\dot{a}$ . Convective and expansion losses are also neglected since the equilibrium is assumed to evolve slowly. The primary diffusive process is assumed to be radial heat conduction and the source terms are assumed to be ohmic power input and bremsstrahlung radiation. Equation (6) reduces to

$$\nabla \cdot \mathbf{q} = \eta_{\perp} j^2 - P_{\text{Brem}} \quad (7)$$

where  $\eta_{\perp}$  is cross-field Spitzer resistivity,  $\eta_{\perp} j^2$  is the ohmic heating term, and  $P_{\text{Brem}}$  is the bremsstrahlung radiation term.

These equations can be simplified by assuming that  $T = T_e = T_i$ , due to the short thermal equilibration time, and  $n = n_e = Z_{\text{eff}} n_i$ , due to the short Debye length, where  $Z_{\text{eff}}$  is the effective charge state of the plasma which is chosen

to be a spatially uniform value of  $Z_{\text{eff}} = 1.33$  for this paper. This value is chosen to account for the 4:1 ratio of hydrogen atoms to carbon atoms in the methane-generated plasma and a spectroscopically observed dominant carbon ionization state of doubly ionized CIII.

The equation for radial force balance is given by

$$\frac{B_\theta}{r} \frac{d(rB_\theta)}{dr} = -\mu_0 k_B \frac{d}{dr} (n_e T_e + n_i T_i). \quad (8)$$

Multiplying both sides of (8) by  $r^2$  and using the chain rule results in

$$\frac{d(rB_\theta)^2}{dr} = c_1 r^2 \left( T \frac{dn}{dr} + n \frac{dT}{dr} \right) \quad (9)$$

where  $c_1 = -2\mu_0 k_B (Z_{\text{eff}} + 1)$ . Equations (7) and (9) must be simultaneously solved to determine the temperature and magnetic field profiles.

By assuming a Fourier-law dependence, the radial heat flux is expressed as

$$q_r = -k_B (\kappa_{\perp e} + \kappa_{\perp i}) \frac{dT}{dr}. \quad (10)$$

Expressions for the thermal conductivity,  $\kappa_{\perp e}$  and  $\kappa_{\perp i}$ , take into account the degree of magnetization of the particles, which is the ratio of the Larmor radius of the particles to the mean free path of the particles. The ion and electron thermal conductivities for the assumed  $Z_{\text{eff}} = 1.33$  are given by [25] as

$$\kappa_{\perp, i} = \frac{nk_B T \tau_i}{Z_{\text{eff}} m_i} \left( \frac{2x_i^2 + 2.645}{x_i^4 + 2.7x_i^2 + 0.677} \right) \quad (11)$$

$$\kappa_{\perp, e} = \frac{nk_B T \tau_e}{m_e} \left( \frac{\gamma_1 x_e^2 + \gamma_0}{x_e^4 + \delta_1 x_e^2 + \delta_0} \right) \quad (12)$$

where the coefficients in the parentheses of 12 are calculated using a third-order fit, as a function of  $Z_{\text{eff}}$ , to the values shown in [25, Table II, p. 251] and the inverse of the magnetization parameters are

$$x_i = \omega_{ci} \tau_i \quad (13)$$

$$x_e = \omega_{ce} \tau_e \quad (14)$$

and  $\omega_{ci}$  is the ion cyclotron frequency,  $\omega_{ce}$  is the electron cyclotron frequency, and  $\tau_i$  and  $\tau_e$  are the collision times of the ions and electrons, respectively

$$\tau_i = 2.09 \times 10^{13} \frac{T^{\frac{3}{2}}}{Z_{\text{eff}}^3 n \ln \Lambda} \quad (15)$$

$$\tau_e = 3.44 \times 10^{11} \frac{T^{\frac{3}{2}}}{Z_{\text{eff}} n \ln \Lambda}. \quad (16)$$

The thermal conductivities given in (11) and (12) take into account the unmagnetized behavior of the particles near the pinch axis where the magnetic field is zero as well as the magnetized behavior near the magnetic field peak.

The Spitzer resistivity term [26] and the bremsstrahlung term [26] are expressed as

$$\eta_{\perp} = 1.035 \times 10^{-4} Z_{\text{eff}} \ln \Lambda T^{-\frac{3}{2}} \quad (17)$$

$$P_{\text{Brem}} = 1.69 \times 10^{-38} Z_{\text{eff}}^2 n^2 T^{\frac{1}{2}}. \quad (18)$$

Using the above equations and definitions, (7), (9), and (10) become [27]

$$\frac{dh}{dr} = \frac{c_1^2 r^3 c_3}{4uT^{\frac{3}{2}}} \left( -\frac{nh}{rk_B(\kappa_{\perp, i} + \kappa_{\perp, e})} + T \frac{dn}{dr} \right)^2 - r P_{\text{Brem}} \quad (19)$$

$$\frac{du}{dr} = c_1 r^2 \left( -\frac{nh}{rk_B(\kappa_{\perp, i} + \kappa_{\perp, e})} + T \frac{dn}{dr} \right) \quad (20)$$

$$\frac{dT}{dr} = -\frac{h}{rk_B(\kappa_{\perp, i} + \kappa_{\perp, e})} \quad (21)$$

where  $c_3 = (1.035 \times 10^{-4} Z_{\text{eff}} \ln \Lambda / \mu_0^2)$ . Auxiliary variables  $h \equiv r q$  and  $u \equiv (rB_\theta)^2$  are defined to simplify the solution procedure.

These equations are solved using a multiple shooting method [28] with the *ode15s* MATLAB routine [29], [30] which is well suited for stiff systems. The boundary conditions are

$$h|_{r=0} = 0 \quad (22)$$

$$u|_{r=0} = 0 \quad (23)$$

$$u|_{r=r_w} = (r_w B_w)^2 \quad (24)$$

where  $r_w$  is the radius of the outer conducting wall and  $B_w$  is the average magnetic field at the wall. Equation (24) is set to match the average magnetic field measured at the outer conducting wall by the probes discussed in Section II-A.

Fig. 11 shows calculated profiles of magnetic field and temperature at three times during the experimental plasma pulse. The shaded areas are the calculated profiles when the measured current centroid location is shifted between  $\pm 1$  mm. The temperature profiles are characterized by a flat profile near the axis due to the high thermal conductivity as a result of weakly magnetized particles. The temperature profile becomes steep further from the axis due to the stronger magnetization of the particles and corresponding low thermal conductivity. The peak temperature is 63 eV at  $t = 49.8 \mu\text{s}$ . This temperature profile, which is broader than the original guess of a Lorentzian profile, coupled with the calculated density profile produces a pressure profile which is broader than the initial guess of a Bennett pressure profile. This broader profile is more stable to the  $m = 0$  mode than the Bennett pressure profile. The magnetic field profile is also noticeably broader with a value of 0.81 T at  $r = a = 0.006$  m and  $t = 49.8 \mu\text{s}$ , and transitions to  $\approx 1/r$  decay after the temperature reaches the minimum value, which is set at  $10^{-3}$  eV. The discontinuity in the magnetic field prior to the  $1/r$  transition is a numerical artifact that is due to the resolution of the solver which results in a discontinuity in the temperature gradient when the temperature reaches the minimum value.

Fig. 12 shows the magnetic field at  $r = a$  and the peak temperature during the quiescent period as a function of time for this pulse. Highlighted by the regression fits, the magnetic field values increase as a function of time to values near 1 T and the temperature increases with peak values of 67 eV for this pulse. Shifting of the measured current centroid location has a greater effect on the peak magnetic field than on the peak temperature. The insensitivity of the temperature to this shift is a direct result of the insensitivity of the calculated linear density.

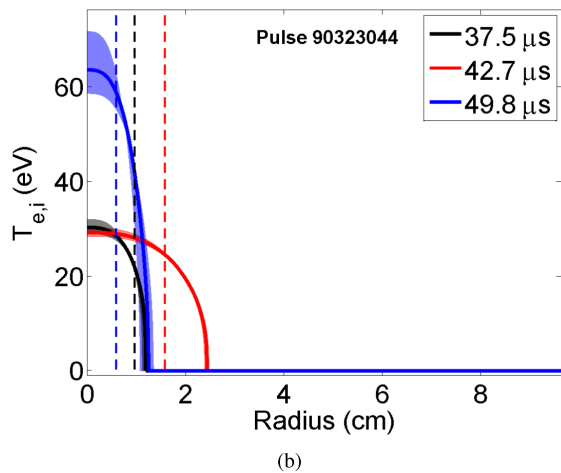
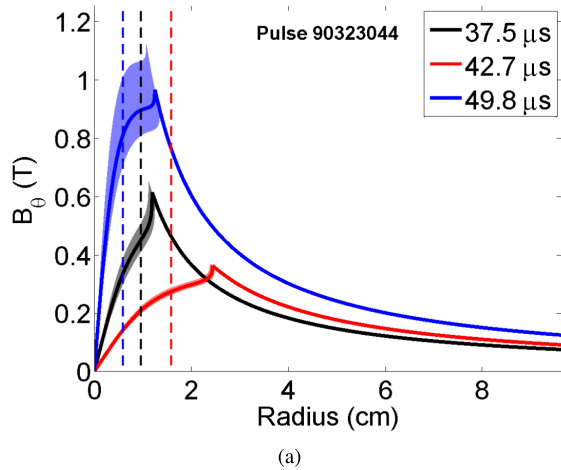


Fig. 11. Magnetic field and temperature profiles for a representative operating conditions at three different times. (a) At  $t = 49.8 \mu\text{s}$ , magnetic field profile has a value of  $0.81 \text{ T}$  at  $r = a = 0.006 \text{ m}$  and is noticeably broader than a Bennett profile. The profile transitions to  $\approx 1/r$  behavior when the temperature profile reaches the minimum value. (b) Temperature profile peaks at  $63 \text{ eV}$  at  $t = 49.8 \mu\text{s}$ . Shaded areas are the calculated profiles with the current centroid displaced between  $\pm 1 \text{ mm}$ . Vertical dashed lines indicate the characteristic radius.

These data combined with the characteristic radius and density data indicate that the pinch undergoes magnetic compression and heating as the quiescent period progresses. These data agree with the interpretation of magnetic compression from Figs. 8 and 9.

Fig. 13 shows contours of the temperature as a function of radius and time during the quiescent period. These contours clearly show the effects of heating through magnetic compression as the quiescent period progresses. These contours are for the calculated profiles for the measured current centroid location only and do not account for the location uncertainty.

## V. SOURCE OF Z-PINCH OSCILLATIONS

The ZaP flow Z-pinch formation process consists of a radial compression from the acceleration region of the experiment to the pinch assembly region. Depending on the radial velocity of the compression, which is dependent on

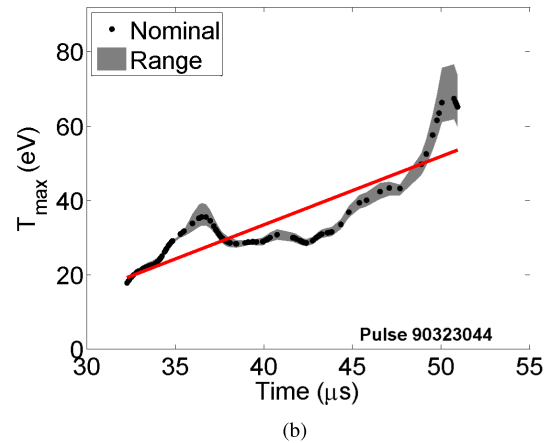
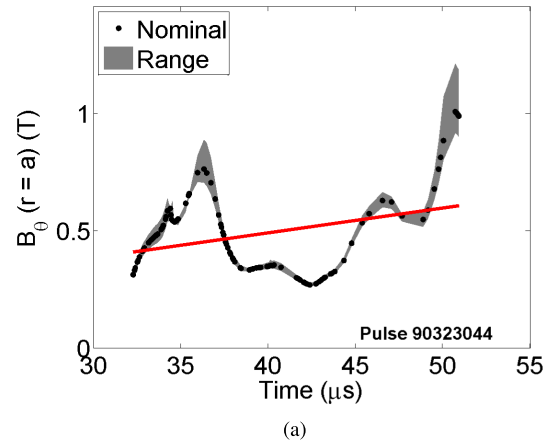


Fig. 12. Magnetic field at  $r = a$  and peak temperature as a function of time for representative operating condition. (a) Magnetic field increases as a function of time. (b) Temperature increases as a function of time in a similar manner to the magnetic field. The magnetic compression results in higher temperatures, peaking at  $67 \text{ eV}$ . The red lines are regression fits of the data to a first-order function in time. Shaded black areas are the calculated peak values with the current centroid displaced between  $\pm 1 \text{ mm}$ .

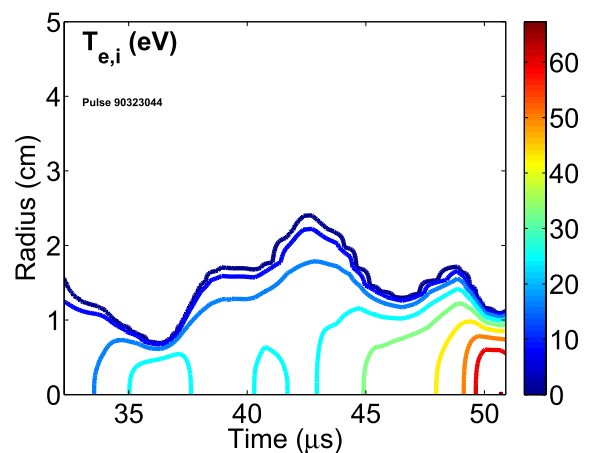


Fig. 13. Temperature contours as a function of radius and time for representative operating condition. As time progresses, the compression and temperature increase of the pinch is observed. Contours are for the calculated temperature profiles for the measured current centroid location only and do not account for the location uncertainty.

the plasma current, the accelerated mass, and the distance over which acceleration occurs, overcompression of the pinch can result whereby the kinetic energy of the plasma

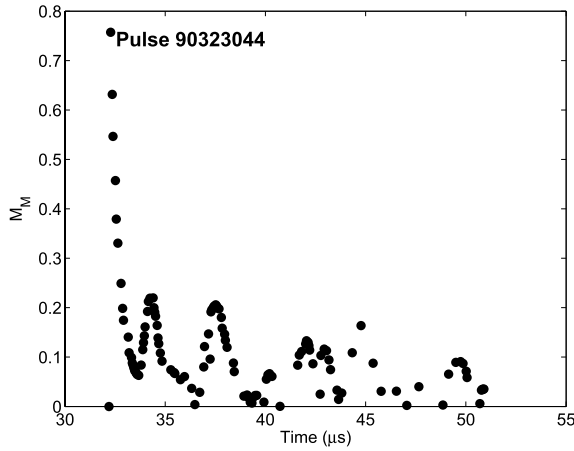


Fig. 14. Magnetic Mach number as a function of time for representative operating condition. The magnetic Mach number remains well below  $M_M = 1.0$  during the pulse, suggesting that equilibration is reached in time scales faster than the characteristic radial motion, justifying the use of a steady-state assumption in the analysis.

may temporarily exceed the magnetic energy resulting in a subsequent expansion [31]. Given constant current conditions, continued oscillations would be expected that are damped due to losses from processes such as radiation. As shown in Fig. 9, the current increases as a function of time, resulting in an overall trend of continued compression of the pinch with the oscillations superimposed as shown in Fig. 8. The time scale of these oscillations (several microseconds) is long compared with the thermal equilibration time of the plasma, validating the assumption of  $T_e = T_i$  in the above analysis.

Furthermore, the radial velocity of the oscillations can be calculated as  $V_r = da/dt$  and compared with the Alfvén velocity,  $V_A$ , through the magnetic Mach number,  $M_M = V_r/V_A$ . This is equivalent to the ratio of the Alfvén time to the characteristic time of radial motion,  $\tau_A/\tau_r$ . The Alfvén velocity is calculated as [26]

$$V_A = \frac{B}{\sqrt{4\pi n_i m_i}} = \frac{B}{\sqrt{4\pi (\frac{1}{6}m_c n_e + \frac{2}{3}m_p n_e)}}. \quad (25)$$

The mean value of  $V_A$  within the characteristic pinch radius is used for this calculation as a conservative estimate. The magnetic Mach number throughout this pulse is always less than 0.22 and typically less than 0.15 as shown in Fig. 14, suggesting that equilibration occurs on time scales faster than the radial motion, justifying the use of a steady-state assumption in the above analysis.

## VI. CONCLUSION

A method to calculate the evolution of the equilibrium properties of a flowing Z-pinch is described. A four-chord He-Ne interferometer was used to measure the electron density profile as a function of time by guessing a Lorentzian electron density profile centered on the measured current centroid of the pinch and fitting the chord-integrated points to the corresponding expression for the chord-integrated profile. The resulting profiles validate a Lorentzian distribution as a

reasonable fit. An azimuthal array of magnetic probes was used to measure the magnetic field at the outer conducting wall of the experiment and the location of the current centroid. The equations of radial force balance and radial heat conduction are then used with these measured parameters to calculate the profiles of temperature and magnetic field in the pinch. The coupled equations are solved with an iterative multiple shooting method, taking into account ohmic heating and bremsstrahlung radiation as sources and sinks, respectively. The analysis method shows that as expected, plasmas in ZaP heat and compress with increasing current suggesting magnetic compression as the quiescent period progresses. Significant oscillations in the size of the pinch are also observed; they are attributed to an initial overcompression of the pinch, due to the formation process, followed by subsequent expansion. Comparison of the equilibration time with the characteristic time of radial motion indicates that equilibration occurs on a faster time scale than the motion, validating the assumption of a steady-state analysis. High thermal conductivity due to weakly magnetized plasma near the axis of the pinch results in a broadened temperature profile that becomes steep near the characteristic radius as the thermal conductivity decreases due to the increasing magnetization of the particles. The analysis method developed is useful for evaluating ZaP pulses from multiple experimental configurations to reconstruct evolving equilibrium profiles and to determine the primary heating mechanisms in the pinch.

This method could also be implemented on other configurations where azimuthal symmetry of the pressure profile can be assumed, such as other pinch devices and FRC's, and the spatial resolution of diagnostics limits the applicability of inversion techniques.

## APPENDIX

EMD [21] operates by reducing a signal into a series of intrinsic mode functions (IMFs). An IMF is a function that satisfies the conditions that the mean value of the function defined by the local maxima and minima is zero and that the number of zero crossings and extrema are equal or differ by no more than one. EMD progresses in a process called sifting in which the IMFs are separated based on their characteristic time scales which are defined by the time lapse between successive extrema [21].

The first IMF identified is the highest frequency IMF, which is subtracted from the original signal and then the sifting process continues on the residual (i.e., original signal without the first IMF). This process continues until the remaining residual is either monotonically increasing or decreasing or constant. Summing all of the resultant IMFs including the monotonic residual returns the original signal meaning that all of the data are retained within the IMFs. An example of an IMF series from interferometry data is shown in Fig. 15. The top plot is the original interferometry signal and the bottom three are IMFs 2–4. Note that as the IMF number increases the frequency of the oscillations decreases.

Each of the IMFs from the interferometry signals has an instantaneous frequency and amplitude that can be determined

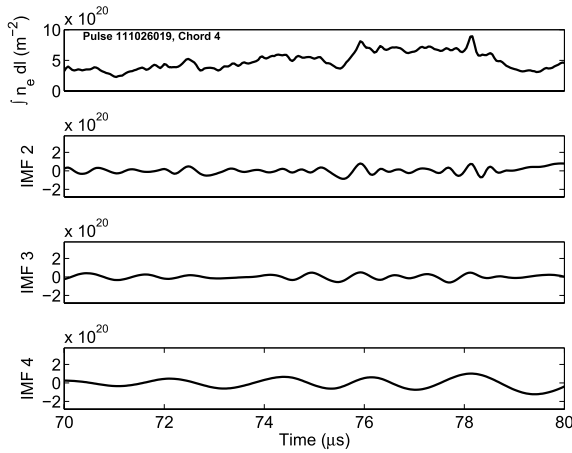


Fig. 15. Example of intrinsic mode functions. EMD breaks down the original signal (topmost plot) into a series of IMFs by defining the highest frequency component in the signal as a function of time (first IMF) and subtracting it from the signal. This process continues until a monotonically increasing or decreasing function is the residual.

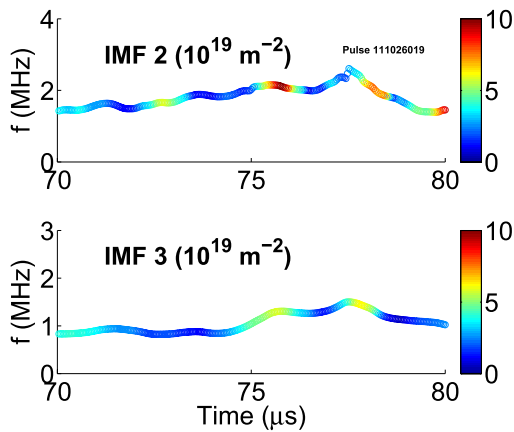


Fig. 16. Hilbert transform of IMFs produces instantaneous frequency and amplitude. The instantaneous frequencies of IMF 2 (top plot) and IMF 3 (bottom plot) for a single chord of interferometry (color indicates instantaneous amplitude) indicate that near 75 and 78  $\mu\text{s}$  there are large amplitude oscillations in the signal with frequencies between 1 and 2 MHz.

by performing a Hilbert transform,  $y(t) = H(x(t))$ , on each IMF

$$y(t) = \frac{1}{\pi} P \int_{-\infty}^{\infty} \frac{x(\tau)}{t - \tau} d\tau \quad (26)$$

where  $P$  signifies the Cauchy principal value of the integral. A complex analytic signal,  $z(t)$ , can now be written

$$z(t) = x(t) + iy(t) \quad (27)$$

which can be expressed as

$$z(t) = x(t) + iy(t) = A(t) \exp(i\psi(t)) \quad (28)$$

where  $i = \sqrt{-1}$  and  $A(t)$  is the instantaneous amplitude of  $z(t)$

$$A(t) = |x(t) + iy(t)| \quad (29)$$

and  $\psi(t)$  is the instantaneous phase

$$\psi(t) = \tan^{-1} \frac{y(t)}{x(t)}. \quad (30)$$

The instantaneous frequency,  $\omega(t)$ , is then defined as

$$\omega(t) = -\frac{d}{dt} \psi(t). \quad (31)$$

The instantaneous amplitude and frequency are plotted as a function of time with a scatter plot as shown in Fig. 16. The vertical axis is frequency, the horizontal axis is time, and the color bar indicates the amplitude. These data indicate large amplitude oscillations near 75 and 78  $\mu\text{s}$  with frequencies between 1 and 2 MHz.

## REFERENCES

- [1] H. Y. Guo, A. L. Hoffman, L. C. Steinhauer, and K. E. Miller, "Observations of improved stability and confinement in a high- $\beta$  self-organized spherical-torus-like field-reversed configuration," *Phys. Rev. Lett.*, vol. 95, p. 175001, Oct. 2005.
- [2] J. Kim *et al.*, "Use of the far infrared tangential interferometer/polarimeter diagnostic for the study of RF driven plasma waves on NSTX," *Rev. Sci. Instrum.*, vol. 81, no. 10, p. 10D527, 2010.
- [3] M. A. Van Zeeland *et al.*, "Conceptual design of the tangentially viewing combined interferometer-polarimeter for ITER density measurements," *Rev. Sci. Instrum.*, vol. 84, no. 4, p. 043501, 2013.
- [4] T. N. Carlstrom, D. R. Ahlgren, and J. Crosbie, "Realtime vibration compensated CO<sub>2</sub> interferometer operation on the DIII-D tokamak," *Rev. Sci. Instrum.*, vol. 59, no. 7, pp. 1063–1066, 1988.
- [5] C. Deng *et al.*, "First results from the multichannel interferometer system on HSX," *Rev. Sci. Instrum.*, vol. 74, no. 3, p. 1625, 2003.
- [6] D. G. Jang, M. S. Kim, I. H. Nam, H. S. Uhm, and H. Suk, "Density evolution measurement of hydrogen plasma in capillary discharge by spectroscopy and interferometry methods," *Appl. Phys. Lett.*, vol. 99, no. 14, p. 141502, 2011.
- [7] A. Case, S. Messer, R. Bomgardner, and F. D. Witherspoon, "Interferometer density measurements of a high-velocity plasmoid," *Phys. Plasmas*, vol. 17, no. 5, p. 053503, 2010.
- [8] E. L. Ruden, S. Zhang, T. P. Intrator, and G. A. Wurden, "Experimental profile evolution of a high-density field-reversed configuration," *Phys. Plasmas*, vol. 13, no. 12, p. 122505, 2006.
- [9] S. L. Jackson and U. Shumlak, "Abel inversion of a holographic interferogram for determination of the density profile of a sheared-flow Z pinch," *Rev. Sci. Instrum.*, vol. 77, no. 8, p. 083502, 2006.
- [10] S. L. Jackson, "Density characteristics of sheared-flow Z-pinch," Ph.D. dissertation, Dept. Aeronautics Astron., Univ. Washington, Seattle, WA, USA, 2006.
- [11] U. Shumlak, R. P. Golingo, B. A. Nelson, and D. J. Den Hartog, "Evidence of stabilization in the Z-pinch," *Phys. Rev. Lett.*, vol. 87, no. 20, p. 205005, 2001.
- [12] U. Shumlak, B. A. Nelson, R. P. Golingo, S. L. Jackson, E. A. Crawford, and D. J. Den Hartog, "Sheared flow stabilization experiments in the ZaP flow Z pinch," *Phys. Plasmas*, vol. 10, no. 5, p. 1683, 2003.
- [13] R. P. Golingo, U. Shumlak, and B. A. Nelson, "Formation of a sheared flow Z pinch," *Phys. Plasmas*, vol. 12, no. 6, p. 062505, 2005.
- [14] U. Shumlak *et al.*, "Equilibrium, flow shear and stability measurements in the Z-pinch," *Nucl. Fusion*, vol. 49, no. 7, p. 075039, 2009.
- [15] G. V. Vogman and U. Shumlak, "Deconvolution of Stark broadened spectra for multi-point density measurements in a flow Z-pinch," *Rev. Sci. Instrum.*, vol. 82, no. 10, p. 103504, 2011.
- [16] J. Marshall, "Performance of a hydromagnetic plasma gun," *Phys. Fluids*, vol. 3, no. 1, pp. 134–135, 1960. [Online]. Available: <http://link.aip.org/link/?PFL/3/134/2>
- [17] U. Shumlak and C. W. Hartman, "Sheared flow stabilization of the  $m = 1$  kink mode in Z pinches," *Phys. Rev. Lett.*, vol. 75, no. 18, pp. 3285–3288, Oct. 1995.
- [18] S. D. Knecht, W. Lowrie, and U. Shumlak, "Effects of a conducting wall on Z-pinch stability," *IEEE Trans. Plasma Sci.*, vol. 42, no. 6, pp. 1531–1543, Jun. 2014.
- [19] U. Shumlak *et al.*, "The sheared-flow stabilized Z-pinch," *Fusion Sci. Technol.*, vol. 61, no. 1, pp. 119–124, Jan. 2012.
- [20] R. P. Golingo, "Modeling magnetic fields measured by surface probes embedded in a cylindrical flux conserver," *Rev. Sci. Instrum.*, vol. 78, no. 3, p. 033504, 2007.
- [21] N. E. Huang *et al.*, "The empirical mode decomposition and the Hilbert spectrum for nonlinear and non-stationary time series analysis," *Proc. Roy. Soc. London A, Math., Phys. Eng. Sci.*, vol. 454, no. 1971, pp. 903–995, 1998.

- [22] W. H. Bennett, "Magnetically self-focussing streams," *Phys. Rev.*, vol. 45, no. 12, pp. 890–897, Jun. 1934.
- [23] J. P. Freidberg, "Ideal magnetohydrodynamic theory of magnetic fusion systems," *Rev. Modern Phys.*, vol. 54, no. 3, p. 801, Jul. 1982.
- [24] J. P. Freidberg, *Plasma Physics and Fusion Energy*, 1st ed. New York, NY, USA: Cambridge Univ. Press, 2007.
- [25] S. I. Braginskii, "Transport processes in a plasma," in *Reviews of Plasma Physics*, vol. 1, M. A. Leontovich, Ed. New York, NY, USA: Consultants Bureau, 1965, pp. 205–311.
- [26] J. D. Huba, "NRL: Plasma formulary," Naval Res. Lab., Washington, DC, USA, Tech. Rep. Rep. NRL/PU/6790-11-551, 2011.
- [27] S. D. Knecht, "Comparison of electrode configurations on ZaP: Investigation of heating mechanisms in a flow Z-pinch," Ph.D. dissertation, Dept. Aeronautics Astron., Univ. Washington, Seattle, WA, USA, 2012.
- [28] J. Stoer and R. Bulirsch, *Introduction to Numerical Analysis*. New York, NY, USA: Springer-Verlag, 1980.
- [29] L. F. Shampine and M. W. Reichelt, "The MATLAB ODE suite," *SIAM J. Sci. Comput.*, vol. 18, no. 1, pp. 1–22, 1997.
- [30] L. F. Shampine, M. W. Reichelt, and J. A. Kierzenka, "Solving index-1 DAEs in MATLAB and simulink," *SIAM Rev.*, vol. 41, no. 3, pp. 538–552, 1999.
- [31] N. G. Kassapakis, H. M. Davies, and M. G. Haines, "One-dimensional simulations of a compressional Z-pinch," *IEEE Trans. Plasma Sci.*, vol. 26, no. 4, pp. 1202–1207, Aug. 1998.



**Sean D. Knecht** (M'14) received the B.S. degree in aerospace engineering from Pennsylvania State University, University Park, PA, USA, in 2005, and the M.S. and Ph.D. degrees in aeronautics and astronautics from the University of Washington, Seattle, WA, USA, in 2008 and 2012, respectively.

He studied experimental plasma physics on the ZaP Flow Z-Pinch Project at the University of Washington. He joined the Applied Research Laboratory, Pennsylvania State University, in 2012, where he is currently a Research Associate. His

current research interests include low-temperature plasma physics and nanoparticle-based photoacoustic biomedical imaging and detection.



**Raymond P. Golingo** received the Ph.D. degree in aeronautics and astronautics from the University of Washington, Seattle, WA, USA, in 2003.

He studied experimental plasma physics on the ZaP Flow Z-Pinch Project at the University of Washington. He is currently a Research Scientist with the University of Washington, where he is involved in the Thomson scattering systems and other diagnostics on the ZaP and TCSU experiments. His current research interests include innovative fusion confinement concepts, electric propulsion, high-energy density plasmas, and new diagnostic techniques.



**Brian A. Nelson** received the Ph.D. degree in nuclear engineering and engineering physics from the University of Wisconsin–Madison, Madison, WI, USA, in 1987.

He is currently a Research Professor with the Department of Electrical Engineering, University of Washington, Seattle, WA, USA. He is also a Secretary/Treasurer with the University Fusion Association and a Chief Technical Officer with Zplasma, Inc., Seattle. He has been involved in experimental and computational plasma physics for

over 30 years. His current research interests include fusion energy, plasma processing, double-layers, solitons, and extreme ultraviolet light emission.



**Uri Shumlak** (M'95) received the Ph.D. degree in nuclear engineering from the University of California at Berkeley, Berkeley, CA, USA, in 1992.

He is currently a Professor of Aeronautics and Astronautics with the University of Washington, Seattle, WA, USA, and the Head of the ZaP Flow Z-Pinch Laboratory and the Computational Plasma Dynamics Group, which leads the development of the WARPX plasma simulation code. He is also the Vice President of the University Fusion Association and a Chief Scientist with Zplasma, Inc., Seattle.

He was a National Research Council Post-Doctoral Fellow with the Air Force Research Laboratory, Kirtland AFB, Albuquerque, NM, USA, where he developed the 3-D, resistive, MHD code, and MACH3. His current research interests include plasma physics, innovative magnetic plasma confinement for fusion energy, high-energy density plasmas, astrophysics, extreme ultraviolet lithography, electric propulsion, and theoretical and computational plasma modeling.